Citation: Vafaie, A., Soler, J.M., Cama, J., Kivi, I.R., Vilarrasa, V., 2024. A MATLAB approach for developing digital rock models of heterogeneous limestones for reactive transport modeling. Geologica Acta, 22.3, 1-14.
DOI: 10.1344/GeologicaActa2024.22.3

geologica acta

A MATLAB approach for developing digital rock models of heterogeneous limestones for reactive transport modeling

Atefeh Vafaie[1] Josep M. Soler[2] Jordi Cama[2] Iman R. Kivi[1] Victor Vilarrasa[3]

[1]Department of Earth Science and Engineering, Imperial College London
Exhibition Rd, South Kensington, London SW7 2AZ, United Kingdom. E-mail: a.vafaie@imperial.ac.uk
Kivi E-mail: i.rahimzadeh-kivi@imperial.ac.uk

[2]Institute of Environmental Assessment and Water Research (IDAEA), CSIC
Jordi Girona, 18-26, 08034 Barcelona, Catalonia, Spain. Soler E-mail: josep.soler@idaea.csic.es.
Cama E-mail: jordi.cama@idaea.csic.es.

[3]Global Change Research Group (GCRG), IMEDEA, CSIC-UIB
Miquel Marquès, 21, 07190 Esporles, Illes Balears, Spain. E-mail: victor.vilarrasa@csic.es

ABSTRACT

Porosity is a key parameter controlling the physico-chemical behavior of porous rocks. Digital rock physics offers a unique technique for imaging the inherently heterogeneous rock microstructure at fine spatial resolutions and its computational reconstruction, through which a better understanding and prediction of the rock behavior can be achieved. In this study, we propose a simple but accurate method to build a 3D porosity map of centimeter-scale carbonate rock cores from X-ray Micro Computed Tomography (XMCT) imaging data. The method consists of 3 main steps: i) decomposition of 3D volumetric XMCT data into sub-volumes, ii) processing of equidistributed 2D cross-section images in each sub-volume and iii) 2D slice-by-slice calculation of porosity and its assembly to reconstruct a 3D continuum porosity map over the whole core domain using a MATLAB code. The proposed approach significantly conserves the required memory to manipulate large image datasets. The digitized porosity representations are used to build 3D permeability maps of the cores by applying an explicit permeability-porosity relationship. The permeability maps are used as input for numerical simulation of the rock response to the percolation of reactive fluids through which the general validity of the approach is verified. The developed digital rock model paves the way for an improved understanding of reactive transport in carbonate rocks.

KEYWORDS **Computed tomography. Digital rock physics. Rock heterogeneity. Porosity reconstruction. Reactive transport modeling.**

INTRODUCTION

Understanding the rock response to Electrical, Thermal, Hydraulic, Mechanical, and Chemical (ETHMC) loading paths is of paramount importance to a variety of geoscience and engineering applications (Rutqvist *et al.,* 2022; Taron and Elsworth, 2009). The rock behavior under diverse loading conditions is controlled by its inherently heterogeneous microstructure (Ju *et al.,* 2014; Li and Benson, 2015). Importantly, the density, distribution, and shapes of the pores and grains largely control macroscopic rock properties (Eberli *et al.,* 2003; Wan and Xu, 2014).

Therefore, a thorough characterization of these properties requires an accurate assessment of relevant microstructural features (Ju *et al.,* 2014; Wan and Xu, 2014). To fulfill this requirement, several imaging techniques, including but not limited to, Scanning Electron Microscopy (SEM), Focused Ion Beam (FIB), and X-ray Micro Computed Tomography (XMCT) have been developed (Ju *et al.,* 2014; Zhang *et al.,* 2016). The XMCT technique, although with a relatively lower spatial resolution compared to SEM and FIB, provides invaluable 3D information on the rock microstructure (Ju *et al.,* 2014; Rabbani *et al.,* 2016, 2019; Wan and Xu, 2014; Zhang *et al.,* 2016).

Digital rock physics, *i.e.* imaging and computing, emerged in the 1990s as a powerful tool for visualizing the internal structure of rocks and inferring effective rock properties from 3D realizations of the rock microstructure (Fredrich *et al.,* 1995; Spanne *et al.,* 1994). Since then, this technology has been increasingly employed as a complementary instrument to conventional core experiments not only for the nondestructive characterization of geomaterials but also for developing a deep understanding of relevant physical processes, mainly involving fluid flow and rock deformation (Andrä *et al.,* 2013). The latter is achieved by numerically simulating physical processes in digital rocks, featuring a representative distribution of relevant properties, and making quantitative comparisons with experimental measurements (Jackson *et al.,* 2018; Rabbani and Jamshidi, 2014). The simulations are commonly carried out at the continuum scale, where the numerical grid cells are based on the concept of Representative Elementary Volumes (REV) comprising a large enough assembly of pores and grains with equivalent properties (Hao *et al.,* 2013; Jackson *et al.,* 2020; Smith *et al.,* 2017). The size of the grids is assigned primarily based on computational costs (in particular for 3D models where the computational time and memory requirements may become exceedingly high for fine grid cells) and constraints on the applicability of physical models. Accordingly, digital rock physics applies statistical or homogenization approaches to derive representative distribution maps of rock properties from microstructural data. These techniques have been successfully used to evaluate a variety of ETHMC properties of rocks (Durán *et al.,* 2019; Ettemeyer *et al.,* 2020; Hao *et al.,* 2013; Smith *et al.,* 2017; Vanorio and Mavko, 2011; Wu *et al.,* 2020). Among them, porosity is a primary parameter that can be derived from the analysis of XMCT data and is also a key input variable to predict other physical rock properties (Eberli *et al.,* 2003).

As digital rock physics gains momentum in geosciences and engineering applications, the need for appropriate approaches to construct 3D image-based maps of rock properties becomes a priority. Such approaches are computationally demanding as they require analyzing large imaging datasets. Here we propose a simple yet computationally efficient and accurate MATLAB-based method to construct a 3D representation of porosity distribution in heterogeneous carbonate rocks. The code is publicly accessible at https://github.com/AVafaie/Porosity-reconstruction-from-CT.git and http://hdl.handle.net/10261/284837. The proposed method includes: i) decomposition of the 3D volumetric image of the rock into equal-size sub-domains, ii) processing of individual, equidistributed 2D images and calculation of porosity along each sub-domain and iii) assembly of slice porosity distribution and mapping onto a 3D continuum rock domain that is defined by arbitrary, user-defined grid sizes and can be used directly in numerical codes. The proposed decomposition of the rock domain and 2D slice-by-slice image processing significantly minimizes computational costs, particularly, in terms of the required memory to handle data, while maintaining accuracy. We also propose a technique to account for sub-CT (Computed Tomography) resolution porosity distribution in the rock. As an example, we used the obtained porosity distribution of a limestone core sample, *i.e.* Pont du Gard Limestone (Vafaie *et al.,* 2023a) to build 3D permeability maps as inputs for CrunchFlow (Steefel and Molins, 2016), an open-access continuum-scale Reactive Transport (RT) code. The proposed procedure can be applied to other problems that require the magnitude and distribution of porosity over porous geomaterials.

METHODS

Image acquisition

The proposed method relies on discretizing the full core XMCT image into smaller sub-volumes along the axis of the rock sample (z-direction). The discretization enables the parallelization of subsequent data processing on sub-volumes, which significantly reduces the computational cost. To this end, the image dataset is opened using the open-access myVGL 2022.4 (data viewer from Volume Graphics Software, see www.volumegraphics.com), and the 3D volumetric image is discretized into an arbitrary number of rectangular cuboid layers (*i.e.* sub-volumes) with the same size along the core axis. Equal-size 2D grayscale cross-section images in which every pixel has an intensity value between 0 and 255 (0 for black and 255 for white) are then exported out of each sub-volume using an equal lengthwise interval. This means that each sub-volume comprises a sequence of equal-size 2D cross-section images separated from each other by a particular distance. To avoid errors in porosity calculations associated with small-scale heterogeneities along the core axis, this distance should be ideally kept at the minimum value equal to the voxel resolution. Excluding the non-rock portions at the bottom and top sides of the images, the remaining cross-section images are exported for each cuboid sub-volume.

Extracted images are first cropped to squares fitting the circular core cross-sections. The images are then segmented (binarized) by applying a global threshold (Otsu thresholding technique, Otsu, 1979; see Porosity distribution of a Pont Du Gard Limestone sample Section) to differentiate the pore network from the solid matrix. The output is a stack of 2D binary images (Fig.1). Accordingly, pixels on the grayscale image having intensities smaller than the threshold value are generally characterized as pores and converted to black pixels on binary images (elements with value 0 in image matrices), while the remaining ones above the threshold represent the solid rock matrix and converted to white pixels on binary images (elements with value 1 in image matrices). The dark air-filled pixels of the region surrounding the core with resembling intensities to pores turn to black pixels after segmentation. This region is then manually converted to solid material (white area) before exporting images to serve as inputs for MATLAB code.

The choice of threshold values is however uncertain and thus intrinsically prone to user perception. Appropriate criteria should be applied to calibrate segmentation. On the one hand, a simple approach is to set the threshold value in a way the measured total porosity equals independent reference measurements (*e.g.* from helium or mercury porosimetry). Nevertheless, this method is well known to result in over-segmentation and unrealistic representation of the rock structure (Berg *et al.*, 2018). On the other hand, the binarization scheme could be optimized through the comparison of a dry scan (air-saturated) image with that of water-saturated rock, as this technique eliminates the need for knowing the CT number of the solid matrix, which is principally unknown (Akin and Kovscek, 2003; Pini and Madonna, 2016). The CT number of a material ($n_{CT\,Mat}$) is defined in the Hounsfield Unit (HU) (Withjack, 1988)

$$n_{CT\,Mat} = 1000\left((\mu_{Mat} - \mu_{Ref})/\mu_{Ref}\right) \quad (1)$$

where μ_{Mat} is the linear X-ray beam attenuation coefficient of the material and μ_{Ref} is the coefficient of a reference material, *i.e.* usually water. Note that CT numbers are projected onto the grayscale level (0 for black and 255 for white) in CT images for illustration purposes.

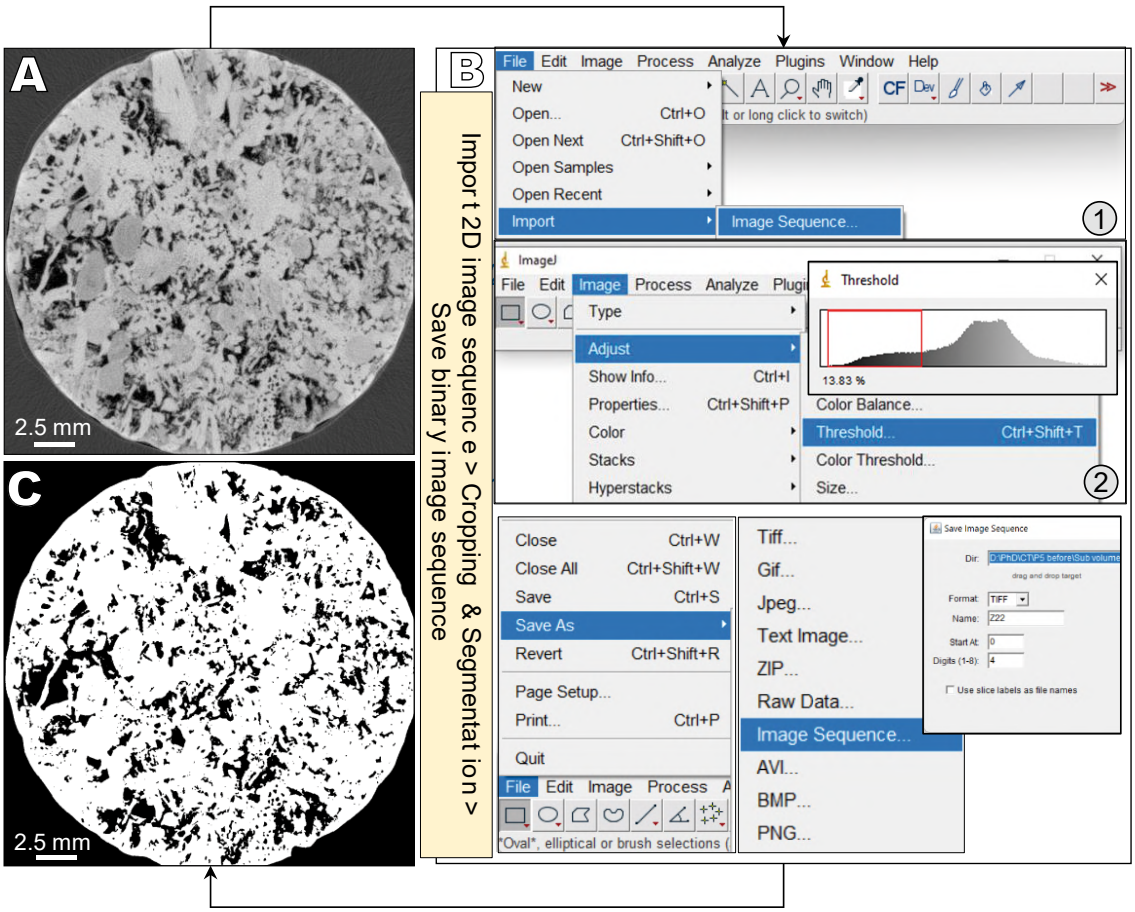

FIGURE 1. A) A 2D XMCT grayscale cross-section image of the Pont Du Gard Limestone, B) flow diagram of adjusting segmentation threshold using the ImageJ software and C) extracted 2D binary images.

We propose here a simple segmentation procedure because more accurate measurements on fluid–saturated samples are not available in this study. This approach includes the application of several automatic algorithms (*e.g.* Renyi Entropy (Kapur *et al.,* 1985), Yen thresholding (Yen *et al.,* 1995), Moments thresholding (Tsai, 1985)) that statistically find optimal threshold values from intensity histograms (indicating how many pixels of each image share the same gray level). We select the best thresholding method by looking for visual similarities in sharp structural features between grayscale and binary images at several points along the core. The same algorithm is applied to all images for the sake of consistency. Pores with sizes less than XMCT image resolution may still result in a significant underestimation of the rock porosity, which is compensated by randomly distributing small pores in the rock matrix (explained in detail in the following sections). All image processing steps are performed in an automated manner using the open-access Java-based ImageJ software (Schneider *et al.,* 2012) (Fig. 1). Note that image segmentation could have also been performed using MATLAB or other suitable programs (Abdulrahman and Varol, 2020; Rabbani and Ayatollahi, 2015). All binarized images from the inlet to the outlet of the core are saved in 8-bit .tif format (Fig. 2), stored in a specified folder, and subsequently used as input files for the MATLAB code (https://github.com/AVafaie/Porosity-reconstruction-from-CT.git and http://hdl.handle.net/10261/284837).

Domain discretization

To build a 3D porosity representation over the core domain using the obtained 2D binarized images, the domain is first discretized into grid cells. The number of grid cells is selected based on the problem of interest. The larger the number (or the smaller the size) of the grid cells, the closer the 3D representation to the actual rock microstructure, but the higher the computational cost. An arbitrary number of cells on the horizontal plane (Cell_X_No and Cell_Y_No) can be assigned, but the number of cells along the core length (Cell_Z_No) equals that of horizontal segments for which binary images were acquired. In this case, we have used a total number of 20 horizontal segments along the core. Yet, there is no restriction on defining more/less horizontal segments based on the problem of interest, the size of the sample, and the CT resolution. This information together with binary 2D images is given as inputs to the code.

Porosity map reconstruction

The code first reads the 2D binary images between the inlet and the outlet of the core but separately and consecutively for the sub-volumes along the core sample. These images are matrices (named IMG in the code) of the same size, in which the number of rows and columns is equal to the number of pixels in the Y and X directions

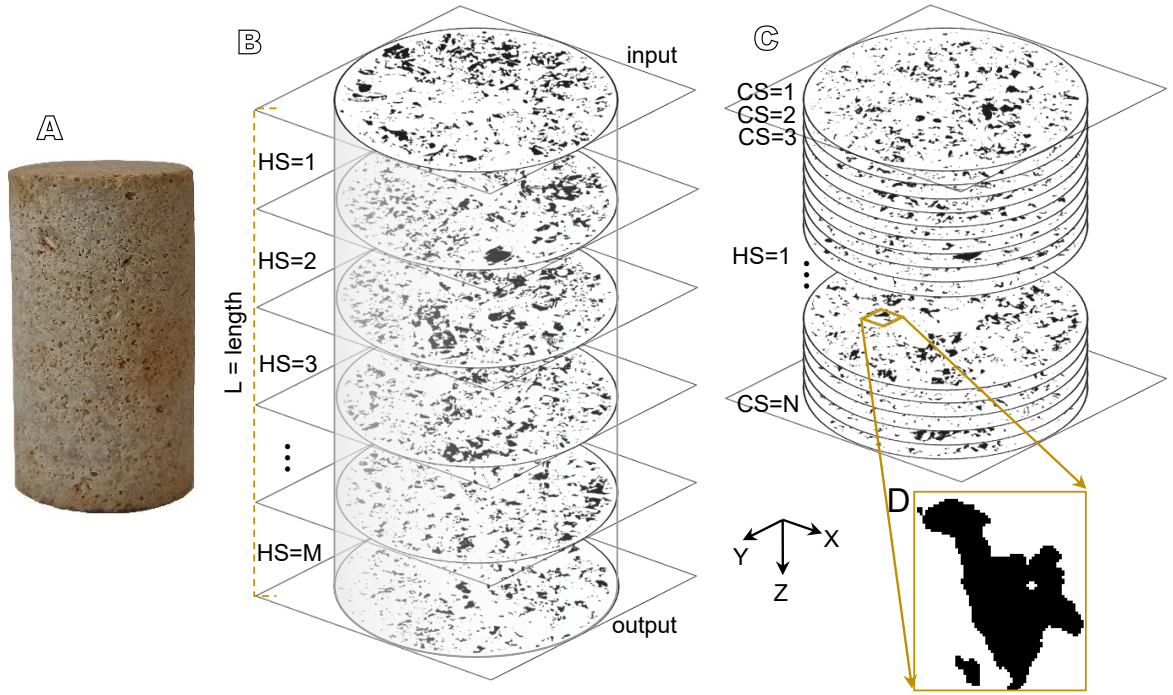

FIGURE 2. A) Photograph of the core of Pont Du Gard Limestone used in this study that comprises 1400×1400×2300voxels with a resolution of 20μm, B) Illustration of the Horizontal Segments (HS) along the core length, C) 2D binary Cross-Section (CS) images in one segment and D) Magnified pixel-based illustration of a pore in a cross-section.

(not necessarily the same), respectively. Each element within these matrices is either 0 or 1, referring respectively to black (pores) and white pixels (solid part) (Fig. 3). The obtained 3D array of binary images in this step is the basis of the 3D porosity reconstruction algorithm.

Figure 4 illustrates the entire workflow of the proposed algorithm, which includes six steps:

1. Locating the core cross-section in the image

Given that 2D binary images are squared, a white marginal area surrounds the circular core cross-section of the core. Image processing starts with diagnosing the image pixels located on the core (named Section_Domain matrix in the code) from those pixels belonging to the marginal area. Assuming that the core cross-section is perfectly circular, the image pixels with a (X, Y) coordinate belong to the rock only if $(X-X_0)^2+(Y-Y_0)^2 \leq r^2$, where (X_0, Y_0) and r are the coordinates of the center and radius of the core, respectively. The rock pixels are set to 1 in the Section_Domain matrix while the pixels of the white marginal area are set to 0.

2. Calculating the average XMCT porosity of the core specimen

The porosity of 2D cross-section images (named Porosity_slice_total in the code) is calculated by dividing the number of pore pixels by the total number of the core cross-section pixels (*i.e.* the sum of Section_Domain elements). The number of pore (0) pixels is obtained by subtracting the sum of solid part (1) pixels in the IMG matrix from the total number of pixels in each image. Subsequently, the average XMCT porosity of each sub-volume (Porosity_zgrid_total in the code) and the whole core (Porosity_total in the code) are derived by calculating the arithmetic mean of the porosity of all images in domains of interest. Note that the calculated porosity accounts for both connected and isolated pores.

3. Modifying XMCT-based porosity (optional)

The average dry XMCT porosity calculated in the previous step may be considerably smaller than the core effective porosity (Por_Eff in the code) measured by other methods. This difference is due to the XMCT resolution that limits the diagnosis of relatively small pores (Mayo *et al.*, 2015; Ramandi *et al.*, 2016). To use the 3D porosity maps in ETHMC numerical simulations, the effective porosity distribution should be first adopted. One should notice that such effective porosity maps accounting for sub-resolution porosity can be directly obtained by processing XMCT images of the rock saturated with a high salinity brine referred to as doped fluid (Lin *et al.*, 2016). The high CT contrast of the fluid with the background mineral(s) enables resolving the effect of tiny pores on the average porosity of the rock. However, this requires integrating a flow-through setup into a XMCT system, which is not frequently available

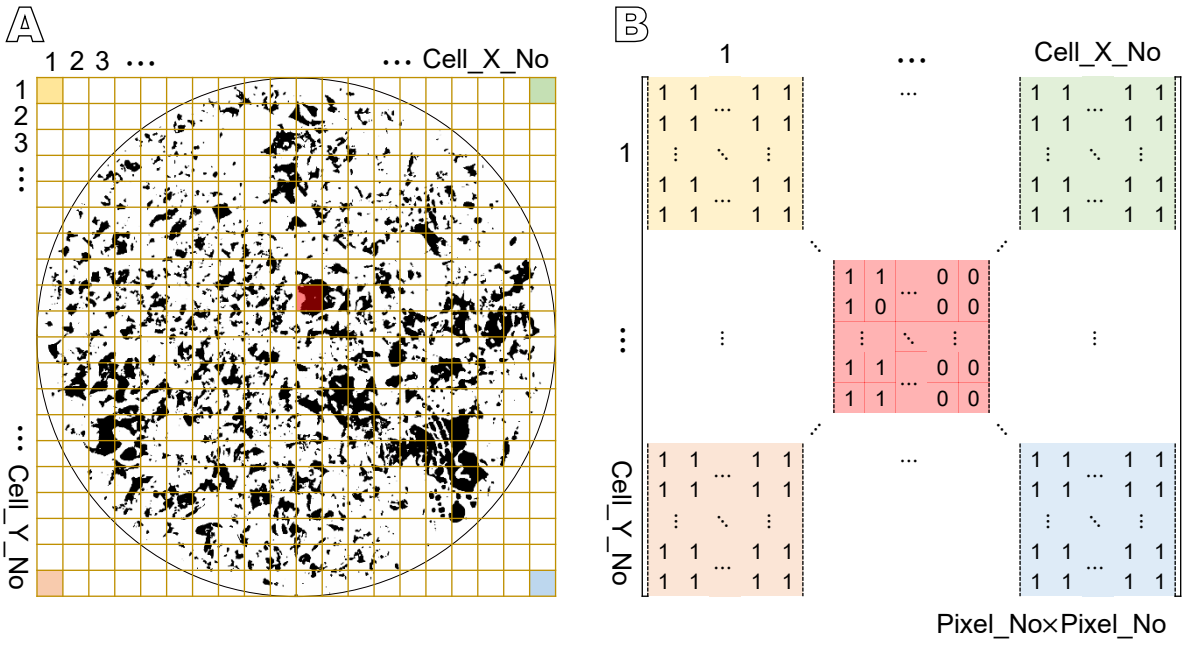

FIGURE 3. A) Illustration of a discretized 2D binary image in X and Y directions and B) the corresponding (0, 1) matrix representation of the image with the size of Pixel_No×Pixel_No.

as it is the case in this study. Thus, we here take into account sub-resolution porosity by adding the difference between the effective porosity and the average XMCT porosity, *i.e.* Porosity_Eff - Porosity_total, to the porosity of each cross-section image. Accordingly, the equivalent number of additional pore elements (Delta_Pixel in the code) is randomly distributed on the solid portion of the core cross-section in 2D binary images. The solid portion of the core cross-sections is identified by dot multiplying (element by element multiplication) IMG and Section_Domain matrices, which returns a matrix of the same dimension with elements equal to 1 denoting the solid portion of the rock.

4. Correlating pixel and grid cell domains

Regardless of the implementation of the porosity modification step, the workflow continues with correlating the pixel domain with the grid cell domain to construct the grid-based porosity map across the core as these two domains have different dimensions. A matrix (Cell_Phi in the code) with the size of Cell_Y_No × Cell_X_No is created for each cross-section image (Fig. 3). Each cell in the Cell_Phi matrix is correlated with a number of pixels in the IMG matrix based on the relative size and coordinates of pixels in cells.

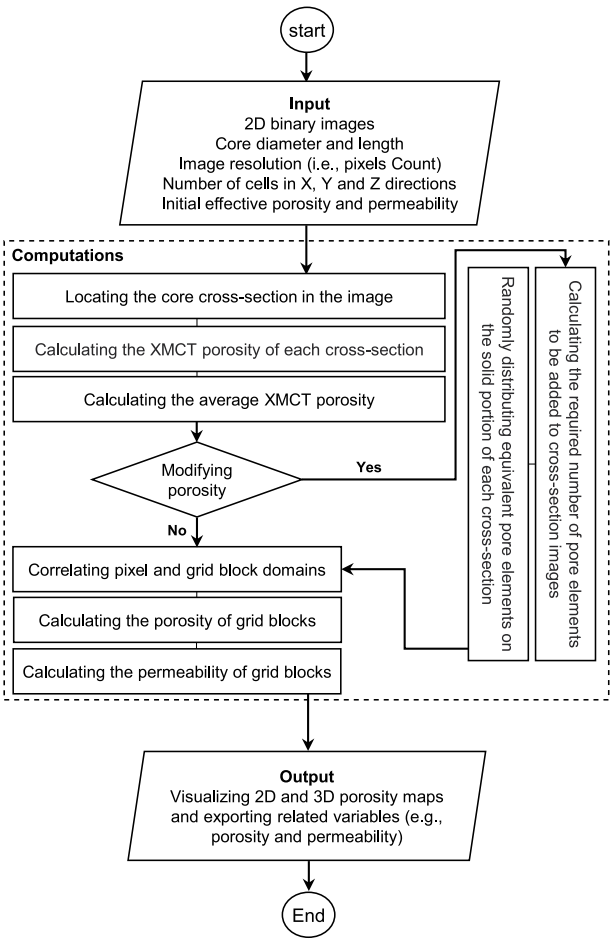

FIGURE 4. Workflow of the algorithm proposed to reconstruct 3D maps of porosity and associated parameters. The algorithm steps are differentiated with numbers located on the left side of the computations section.

5. Calculating the porosity of grid cells

The porosity of each grid cell is calculated using the same logic as in step 2, *i.e.* by counting the number of the pore (0) elements and dividing it by the total number of elements occupying each cell. It is worth noting that the zero-porosity grid cells (white marginal area) surrounding the core form a non-reactive, impervious zone in our RT simulations and help to impose appropriate boundary conditions. However, these elements are excluded for illustration purposes.

6. Visualizing and exporting the 3D porosity map

Following the calculation of porosity in grid cells of each sub-volume, an output 2D array (Porosity_2D in the code) is defined to store (X, Y) coordinates of the centers of the cells and their corresponding porosities. These matrices are then used to plot grid-based porosity distribution maps in each segment. The higher the Cell_Y_No and Cell_X_No, the more precise the porosity representation map. The compilation of porosity distribution matrices for 2D cross-sections (Porosity_2D in the code) is used to construct the 3D porosity map of the core. Several options are provided to create different 2D and 3D porosity maps. 3D arrays of all initial and adjusted binary images, porosity distribution on the grid domain, and grid information are exported for further analyses.

RESULTS

Porosity distribution of a Pont Du Gard Limestone sample

The described image processing approach for 3D XMCT data is applied to a dry Pont Du Gard Limestone core (diameter of 25mm and length of 44mm). The grayscale image of the rock volume, previously reconstructed from the X-ray CT radiographs, comprises 1400×1400×2300voxels with a resolution of 20μm and is represented by a dataset of 8-bit unsigned integers with an approximate size of 4.5GB. The dataset is discretized into 20 sub-volumes along the core axis, and 108 cross-section images are exported at a section-to-section distance of 20μm (*i.e.* the voxel resolution) for each sub-volume. Cropping images to squares fitting the cylindrical core yields cross-sections containing 1250×1250pixels, *i.e.* Pixel_No=1250.

As for the segmentation, the Otsu thresholding technique (Otsu, 1979) returns reliable realizations of the rock structure. This technique selects appropriate thresholds from gray-level histograms by minimizing the intra-class intensity variance or equivalently by maximizing the inter-class intensity variance (σ^2) as

$$\sigma^2 = w_p \times w_s \times (\mu_p - \mu_s)^2 \quad (2)$$

where σ^2 is the inter-class variance and μ is the average value of intensities weighted by w as the number of pixels occupying the corresponding intensity range. Indices p and s point to pore (intensities smaller than the threshold) and solid (intensities larger than the threshold) classes, respectively.

As a representative example, Figure 5 depicts cross-section images of the core sample (Fig. 5A, B), the corresponding gray-level histogram and the evolving inter-class variance (Fig. 5C). Two sharp peaks and a wide valley in between are recognized in the histogram. Note that the first peak includes both the pore region and the air-filled dark region surrounding the core. In particular, it is widely recognized that the Otsu approach performs well when the histogram features a bimodal distribution with sharp peaks (Kittler and Illingworth, 1985). The inter-class variance peaks at 109 (Fig. 5C) indicate that intensities larger than this threshold serve as the solid rock mineral, whereas the smaller gray levels point to either pores or the surrounding air-filled region. After applying segmentation, the 2D grayscale images are transformed into binarized images in which the pore and the air-filled surrounding region pixels are black and solid matrix pixels are white (Fig. 5B). The black surrounding region is then manually converted to white (solid matrix) before exporting binarized images (not shown in Fig. 5) to be used in MATLAB code as explained in the image acquisition section.

The core domain is uniformly discretized into 20×20×20 grid cells, corresponding to a grid width of 1.25mm in the X and Y directions and a length of nearly 2.2mm in the Z direction. Each grid cell thus contains 62×62×108voxels at the original CT resolution (20μm). The variation of computed XMCT porosity along the length of the limestone sample is shown in Figure 6, highlighting the heterogeneous nature of the rock structure. The average porosity over the grid cells satisfactorily captures the microstructural patterns rendered by the high-resolution cross-section images. The initial CT porosity (blue curves in Fig. 6) varies between 0.1 to 0.16 with an average of 0.13, suggesting that the imaging approach underestimates the bulk rock porosity (0.24) by 0.11 units. This underestimation originates from the resolution of the CT imaging technique by which a considerable portion of relatively small pores (<20μm) cannot be diagnosed. The observed porosity layering pattern is reproduced by the adjusted porosity (brown curves in Fig. 6) owing to the adopted porosity updating strategy of adding uniformly the porosity difference of 0.11 to all cross-section images. It should be noted that comparison with the effective rock porosity is subject to the assumption that the volume fraction of isolated pores in the Pont Du Gard Limestone is negligible.

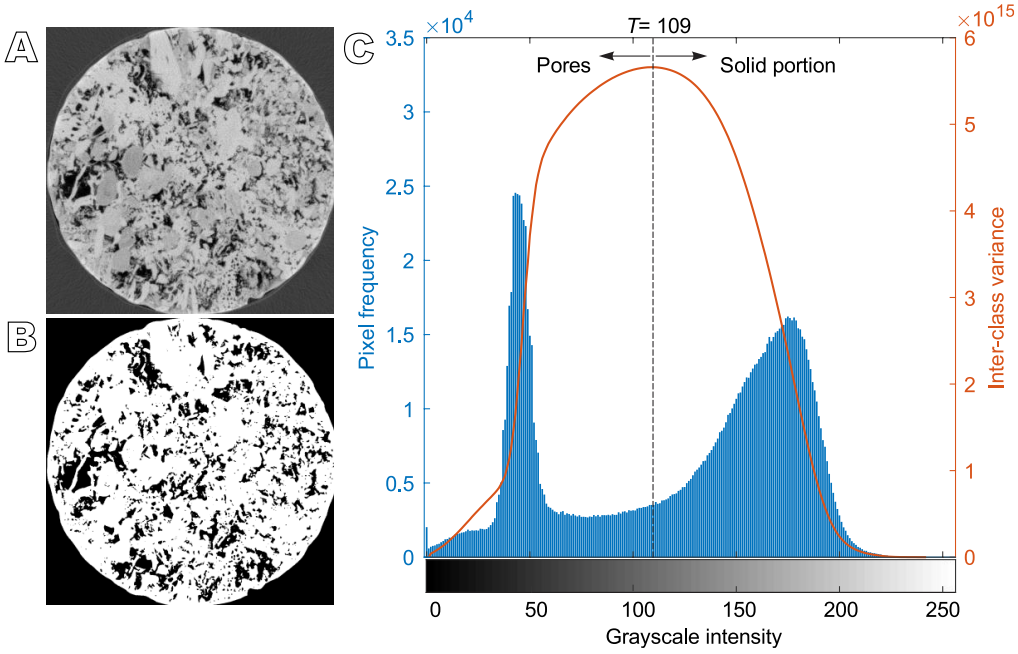

FIGURE 5. Pont du Gard Limestone core: A) 8-bit gray-level cross-section image from the XMCT data, B) corresponding binary image with a size of 1.49MB and C) the segmentation procedure based on the Otsu method.

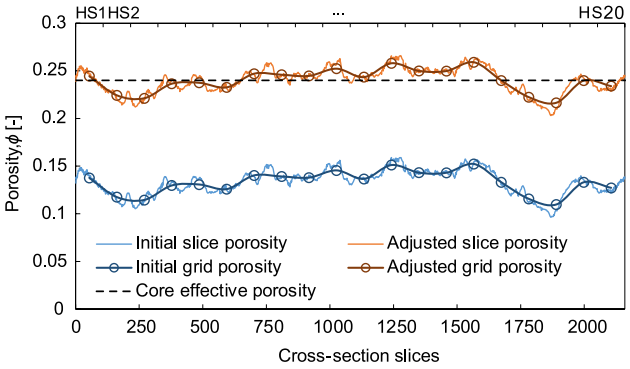

FIGURE 6. Workflow of the algorithm proposed to reconstruct 3D maps of porosity and associated parameters. The algorithm steps are differentiated with numbers located on the left side of the computations section.

Figure 7 illustrates the porosity adjustment procedure for a single image with general validity for the whole sample. Adding the pores randomly at pixel level results in uniform porosity enhancement across the rock slice (compare the subplots in the two rows of Fig. 7). While image processing initially classifies the rock as non-porous in different possible grid cells (subplots on the top row), adjusted images point to a porous background accounting for sub-resolution porosity, *i.e.* pores <20μm (subplots on the bottom row). The grid-based porosity distribution maps with 20×20 grid cells satisfactorily reproduce the structural features observed in binary images, especially the distribution of large pores that could contribute to flow localization. Further refinement of the grid (40×40) significantly increases the accuracy of the porosity distribution map. Grid refinement, however, increases the computational cost for numerical simulations built on the extracted porosity maps.

The heterogeneous distribution of porosity over the examined core can be also inferred from the 3D porosity map constructed by image processing and the corresponding frequency distribution (Fig. 8). The extracted porosity map yields a mean value of 0.217 with a standard deviation of 0.102. The mean porosity of the digital rock at a large grid size is smaller than the effective rock porosity (0.238). This is due to the square-edged shape of the grid domain that deviates from the cylindrical core shape and adds to the real bulk rock volume. Mean digital rock porosities of 0.227, 0.231, 0.233, and 0.235 were calculated for 40×40, 60×60, 80×80, and 100×100 grid schemes perpendicular to the core axis with always 20 grids along the core axis, respectively. The larger the number of grid cells, the closer the grid domain shape to

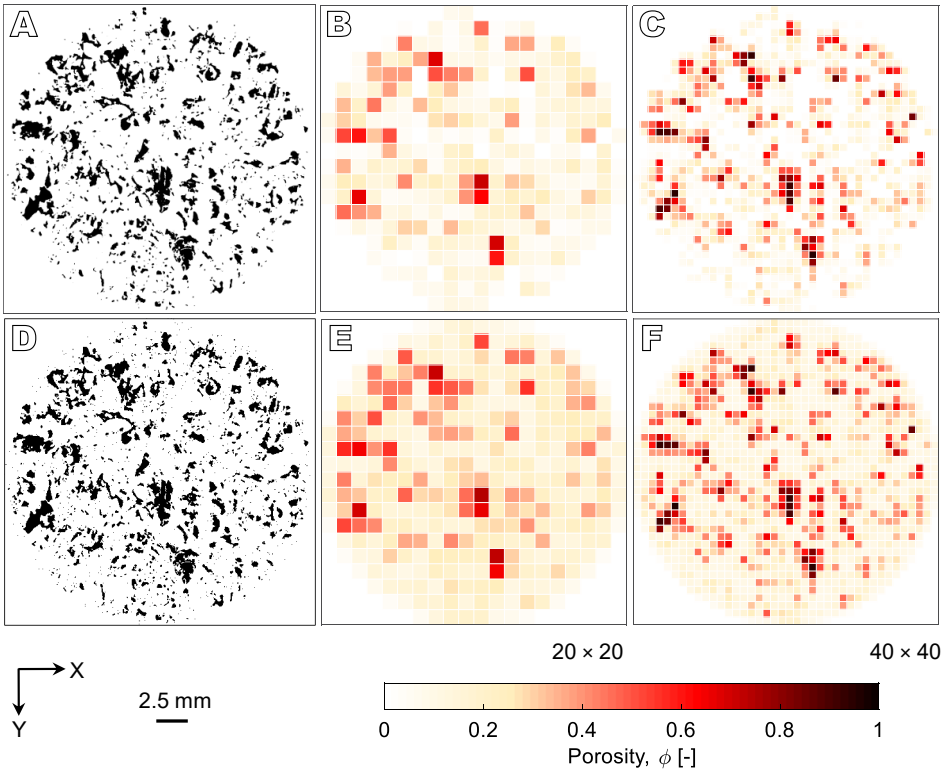

FIGURE 7. 2D illustrations of: A) a raw binary cross-section image, B) a reconstructed grid-based porosity map with a size of 20×20 cells and C) a reconstructed grid-based porosity map with a size of 40×40 cells. Similar plots D, E and F) provided for the cross-section after adjusting the XMCT porosity to effective porosity from bulk porosimetry.

a cylinder and the more accurate the calculated mean grid porosity.

Code performance

The described image processing steps were implemented in MATLAB version 2010b and run on a quad-core Intel Core i7-4790 (up to 3.6GHz) with a maximum of 8GB RAM. The total runtime was 211s, divided by 57.7s for importing and calculating porosity for all images, 130.2s for adjusting the calculated porosity to the effective porosity obtained from mercury porosimetry, 6.4s for building porosity maps on the grid cell domain of 20×20 size, and 16.8s for calculating permeability maps (as described in the application to reactive transport modeling section) and exporting data for further analyses. MATLAB used a total memory of less than 750MB to perform all calculations. The code can be further optimized to conserve more memory and make processing larger datasets affordable with low-power computational resources.

APPLICATION TO REACTIVE TRANSPORT MODELING

In this section, we discuss the application of the developed digital rock model to reactive transport modeling of an experiment, in which an acidic solution (CO_2-saturated water) percolated through a Pont du Gard Limestone core. The experimental results were reproduced by 3D Darcy-scale reactive transport modeling using the CrunchFlow code (Dávila *et al.,* 2021; Steefel and Molins, 2016; Steefel *et al.,* 2015). This code can consider the spatial distribution of porous rock properties (*i.e.* porosity, permeability and tortuosity) when solving fluid flow, solute transport and multicomponent equilibrium and kinetic reactions in porous rock media (Steefel *et al.,* 2015). It should be noted that our numerical grid size (1.25×1.25×2.2mm^3) is much larger than the largest pore throat size measured by the MICP test to be ≈100μm (Vafaie *et al.,* 2023a). Thus, numerical cells well represent the average properties of the involved microstructural features and allow considering their effect on flow, transport, and reaction processes, a gap in conventional simulation workflows (Hao *et al.,* 2013; Smith *et al.,* 2017; Wenck *et al.,* 2021). CrunchFlow uses a single-column format .txt file for initial rock properties in each direction (3 files in 3D problems). The input files consist of one value per line, specifying a rock property (*e.g.* porosity, permeability) in one single grid cell (see Steefel and Molins, 2016, for a detailed explanation of the file formats).

We use the 3D grid-based porosity map to build the single-column-format permeability files (PermX, PermY, and PermZ in the code) for the studied limestone core. The initial permeability of each grid cell from the corresponding porosity was calculated using the Kozeny-Carman cubic law, which is expressed as

$$k_i = k_{eff} \frac{\left(\phi_i / \phi_{eff}\right)^3}{\left((1-\phi_i)/(1-\phi_{eff})\right)^2} \quad (3)$$

where k_i and ϕ_i are the initial permeability and porosity of the grid cell i in the core domain, and k_{eff} and ϕ_{eff} are the effective porosity and permeability of the core, respectively, measured by appropriate laboratory techniques and supplied as input values to the code (Fig. 4). It should be noted that the Kozeny-Carman relationship is supposed to work well for intact rocks when strong modifications in the porosity and pore structure do not occur. To demonstrate the validity of this relationship for our rock sample, we

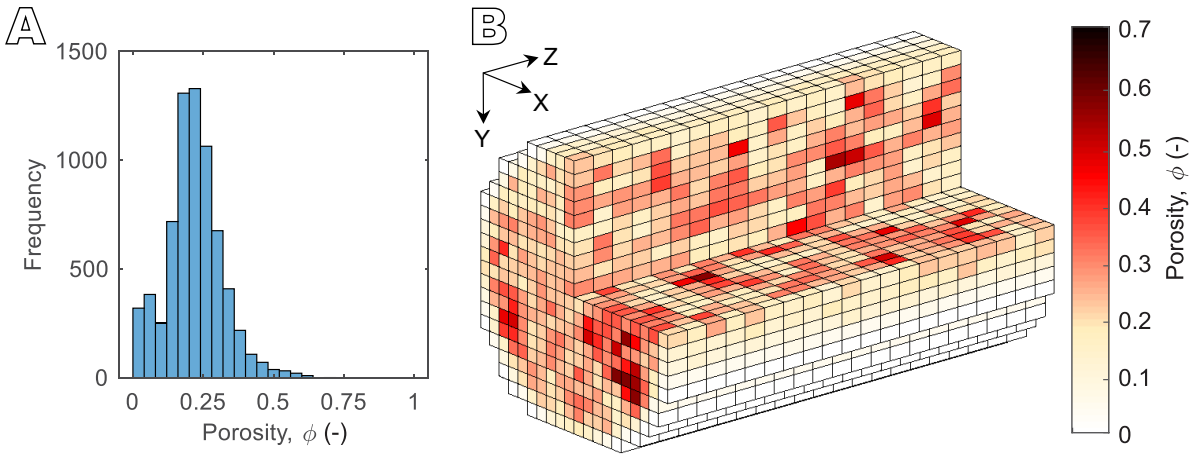

FIGURE 8. Heterogeneous distribution of porosity over the examined core: A) histogram showing the grid-based distribution of total porosity obtained from image processing and B) 3D porosity map with the size of 20×20×20 grid cells for Pont Du Gard Limestone core.

have used the generated permeability map to reproduce the initial bulk permeability of the core. Interestingly, the higher or lower n values cause deviations of the estimated bulk permeability from the experimentally measured value. Indeed, using the same k_{eff} (measured experimentally for the bulk rock permeability), but different n exponents in the porosity-permeability relationship (Eq. 3) generates different realizations of the initial permeability distribution and the numerically calculated bulk flow across the rock.

The extracted permeability maps in the CrunchFlow code were used to assess the influence of rock heterogeneity on the reactive flow of CO_2-saturated water in the limestone core during a percolation experiment (see Vafaie *et al.,* 2023a for detailed information). In this experiment, the CO_2-saturated water with a pH of ≈3.13 ([CO_2 (aq)]= 1.03mol/kg_H_2O) was injected into the core for 28 days at a constant flow rate of 0.15mL/min and a constant pressure and temperature (100bar and 60°C, Vafaie *et al.,* 2023a). XMCT observations after injection revealed a significant increase in bulk rock porosity ($\Delta\phi \approx 13.8\%$) due to calcite dissolution (Fig. 9A, B), leading to wormhole formation in response to the initial heterogeneity of the rock (Vafaie *et al.,* 2023a, b).

In the numerical simulation, the initial and boundary conditions in numerical simulations are considered identical to those of the experiment: i) no-flow lateral boundaries, ii) constant pressure at the outlet and iii) constant flow rate at the inlet under constant temperature conditions during the experiment. Rate laws and reaction rate constants (inputs for simulations) are those given by Dávila *et al.* (2015). A power-law porosity-permeability relationship, similar format to the Kozeny-Carman cubic law (Eq. 3), is used to calculate the evolution of permeability with porosity changes (Hommel *et al.,* 2018)

$$k = k_i \left(\phi/\phi_i\right)^n \cdot \left((1-\phi_i)/(1-\phi)\right)^2 \quad (4)$$

where ϕ and k are porosity and permeability for each grid cell, respectively, and ϕ_i and k_i are initial porosity and permeability values, respectively. Note that the initial rock heterogeneity is exclusively considered in the permeability map. Thus, ϕ_i is constant and equals the effective rock porosity in all cells. The exponent n is an empirical parameter against which the model is calibrated to reproduce the structure of the formed wormhole.

By setting n=15 (Eq. 4), simulations satisfactorily reproduce the composition of the solution at the outlet of the rock core (not shown here) and both the porosity enhancement in the reacted limestone and the structure and orientation of the created wormhole (Fig. 9C). The large n value, which increases the sensitivity of permeability to porosity changes, is necessary to reproduce the strong feedback between flow and mineral dissolution resulting in fluid channeling and wormhole creation. The obtained exponent value is consistent with reported values for carbonate rocks used to simulate the injection of acidic fluids into these rocks (Hao *et al.,* 2019; Hao *et al.,* 2013; Smith *et al.,* 2017; Voltolini and Ajo-Franklin, 2019).

Figure 10 shows histograms of permeability distribution across the core sample before and after the percolation experiment. It is observed that upon interaction with CO_2-saturated water, permeability largely increases (by orders of magnitudes) corresponding to the large n value of 15 in

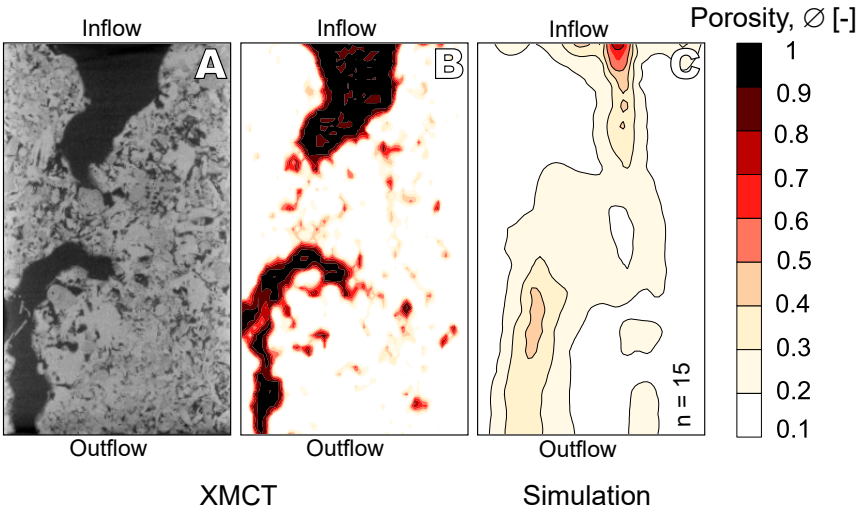

FIGURE 9. Dissolution pattern in the Pont du Gard Limestone core after percolation with CO_2-saturated water: A) grayscale XMCT cross-section of the reacted core representing pore space distribution (black areas) featuring a wormhole structure, B) porosity map of the same cross-section, and C) RT simulation of the porosity distribution in the same cross-section capturing wormhole formation.

Equation 4. Permeability values in grid cells of the altered rock span a wide yet generally reasonable range. There is only a small number of cells near the core inlet (nearly 40 cells out of the whole rock domain) in which permeability reaches a very high value in the order of $10^{-5}m^2$ as a result of the large porosity increase that they experienced. We can approximate the permeability of these cells in the wormhole region using the Poiseuille–Hagenbach equation for a tube (Sutera and Skalak, 1993). If the tube diameter equals the cell width (=1.25mm), the Poiseuille–Hagenbach equation yields a permeability of $5\times10^{-8}m^2$ for each cell, which is comparable to those predicted using a power-law relationship with n=15 in our model. This difference could be even smaller for a planar array of high-porosity cells forming the wormhole cross section as the Poiseuille–Hagenbach permeability scales with the square of wormhole diameter. Moreover, the effect of the above-mentioned very high-permeability cells on the overall simulation results is minimal as these cells constitute a very small portion of the total numerical cells within the rock.

Overall, the ability of the model to capture the rock response to the percolation of the acidic solution demonstrates that although the model is simple compared to other modeling approaches, *e.g.* the use of the Navier-Stokes equation or a combination of the Navier-Stocks equation with the Darcy equation (Panga *et al.,* 2005; Liu and Liu, 2016; De Paulo Ferreira *et al.,* 2020), it yields a reliable predictive performance. Nevertheless, a better match with experimental data may be achieved by refining the mesh and analysis of the parameters controlling the flow and reaction front advance in the studied limestone. The constructed initial permeability maps exhibit the small-scale heterogeneities of the limestone core leading to the localization of flow and reaction. The model can properly capture the structure of the dissolution pattern indicating the general validity of the proposed MATLAB code to obtain the initial porosity and permeability maps.

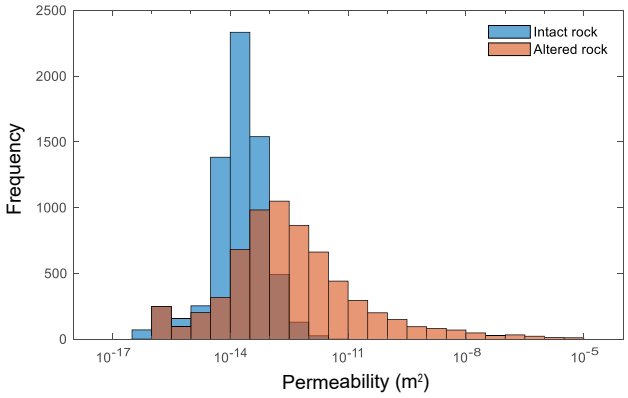

FIGURE 10. Histograms of the grid-based permeability distribution in the intact (blue color bins) and altered limestone core (apricot color bins).

CONCLUSIONS

In this study, we have developed a MATLAB-based approach to quantify and visualize the distribution of porosity in limestones (or other similar rocks) from XMCT images. The method has been applied to a core from the Pont Du Gard Limestone. The code implements the image processing procedure at a low computational cost, which is affordable by standard desktop computers. A good correspondence is obtained between measurements at the voxel scale and model grid domains in terms of both bulk rock porosity and spatial pore distribution. The finer the grid size, the more accurate the continuum-scale porosity maps. Overall, the digital rock realizations allow the study of the heterogeneous structure of the Pont du Gard Limestone sample reacted with CO_2-rich water. We demonstrate the applicability and validity of the proposed approach by parameterizing a continuum 3D Darcy-scale reactive transport model of CO_2-rich water injection into a core sample to reproduce the dissolution pattern formed in the experiment. The developed methodology effectively brings together digital rock physics and Darcy-scale reactive transport modeling. This combination should enable improvements in our understanding and upscaling of geochemical interactions between fluids and rocks, which is fundamental for the optimization and risk assessment of geo-energy applications.

ACKNOWLEDGMENTS

This work has received funding from the Catalan Government through project 2021 SGR 00308 and Shell through the InFUSE Prosperity Partnership. I.R.K. acknowledges support by the PCI2021-122077-2B project (www.easygeocarbon.com) funded by MCIN/AEI/10.13039/501100011033 and the European Union NextGenerationEU/PRTR. I.R.K. also acknowledges funding from the Engineering and Physical Sciences Research Council through the UKRI Postdoc Guarantee Award THMC4CCS [Grant number EP/X026019/1]. V.V. acknowledges funding from the Spanish Ministry of Science and Innovation through the project HydroPore (PID2019-106887GB-C32). IDAEA-CSIC is a Centre of Excellence Severo Ochoa (Spanish Ministry of Science and Innovation, Project CEX2018-000794-S funded by MCIN/AEI/10.13039/501100011033). This research has been carried out within the framework of the activities of the Spanish Government through the "Maria de Maeztu Centre of Excellence" accreditation to IMEDEA (CSIC-UIB) (CEX2021-001198).

REFERENCES

Abdulrahman, A., Varol, S., 2020. A review of image segmentation using MATLAB environment. Beirut (Lebanon), 2020 8th International Symposium on Digital

Forensics and Security (ISDFS), IEEE, 1-5. DOI: 10.1109/ISDFS49300.2020.9116191

Akin, S., Kovscek, A.R., 2003. Computed tomography in petroleum engineering research. London, The Geological Society, 215(1, Special Publications), 23-38. DOI: https://doi.org/10.1144/GSL.SP.2003.215.01.03

Andrä, H., Combaret, N., Dvorkin, J., Glatt, E., Han, J., Kabel, M., Keehm, Y., Krzikalla, F., Lee, M., Madonna, C., Marsh, M., 2013. Digital rock physics benchmarks—Part I: Imaging and segmentation. Computers & Geosciences, 50, 25-32. DOI: https://doi.org/10.1016/j.cageo.2012.09.005

Berg, S., Saxena, N., Shaik, M., Pradhan, C., 2018. Generation of ground truth images to validate micro-CT image-processing pipelines. The Leading Edge, 37(6), 412-420. DOI: https://doi.org/10.1190/tle37060412.1

Dávila, G., Luquot, L., Soler, J.M., Cama, J., 2015. 2D reactive transport modeling of the interaction between a marl and a CO_2-rich sulfate solution under supercritical CO_2 conditions. International Journal of Greenhouse Gas Control, 54, 145-159. DOI: https://doi.org/10.1016/j.ijggc.2016.08.033

Dávila, G., Cama, J., Chaparro, M.C., Lothenbach, B., Schmitt, D.R., Soler, J.M., 2021. Interaction between CO_2-rich acidic water, hydrated Portland cement and sedimentary rocks: Column experiments and reactive transport modeling. Chemical Geology, 572, 120122. DOI: https://doi.org/10.1016/j.chemgeo.2021.120122

De Paulo Ferreira, L., Surmas, R., Tonietto, S.N., Pereira da Silva, M.A., Pires Peçanha, R., 2020. Modeling reactive flow on carbonates with realistic porosity and permeability fields. Advances in water resources, 139, 103564. DOI: https://doi.org/10.1016/j.advwatres.2020.103564

Durán, E.L., Adam, L., Wallis, I.C., Barnhoorn, A., 2019. Mineral alteration and fracture influence on the elastic properties of volcaniclastic rocks. Journal of Geophysical Research: Solid Earth, 124(5), 4576-4600. DOI: https://doi.org/10.1029/2018JB016617

Eberli, G. P., Baechle, G. T., Anselmetti, F. S., Incze, M. L., 2003. Factors controlling elastic properties in carbonate sediments and rocks. The Leading Edge, 22(7), 654-660. DOI: https://doi.org/10.1190/1.1599691

Ettemeyer, F., Lechner, P., Hofmann, T., Andrä, H., Schneider, M., Grund, D., Volk, W., Günther, D., 2020. Digital sand core physics: Predicting physical properties of sand cores by simulations on digital microstructures. International Journal of Solids and Structures, 188, 155-168. DOI: https://doi.org/10.1016/j.ijsolstr.2019.09.014

Fredrich, J.T., Menéndez, B., Wong, T.F., 1995. Imaging the pore structure of geomaterials. Science, 268(5208), 276-279. DOI: 10.1126/science.268.5208.276

Hao, Y., Smith, M., Sholokhova, Y., Carroll, S., 2013. CO_2-induced dissolution of low permeability carbonates. Part II: Numerical modeling of experiments. Advances in water resources, 62, 388-408. DOI: https://doi.org/10.1016/j.advwatres.2013.09.009

Hao, Y., Smith, M.M., Carroll, S.A., 2019. Multiscale modeling of CO_2-induced carbonate dissolution: From core to meter scale. International Journal of Greenhouse Gas Control, 88, 272-289. DOI: https://doi.org/10.1016/j.ijggc.2019.06.007

Hommel, J., Coltman, E., Class, H., 2018. Porosity–permeability relations for evolving pore space: a review with a focus on (bio-) geochemically altered porous media. Transport in Porous Media, 124(2), 589-629. DOI: https://doi.org/10.1007/s11242-018-1086-2

Jackson, S.J., Agada, S., Reynolds, C.A., Krevor, S., 2018. Characterizing drainage multiphase flow in heterogeneous sandstones. Water Resources Research, 54(4), 3139-3161. DOI: https://doi.org/10.1029/2019WR026396

Jackson, S.J., Lin, Q., Krevor, S., 2020. Representative elementary volumes, hysteresis, and heterogeneity in multiphase flow from the pore to continuum scale. Water Resources Research, 56(6), e2019WR026396. DOI: https://doi.org/10.1029/2019WR026396

Ju, Y., Zheng, J., Epstein, M., Sudak, L., Wang, J., Zhao, X., 2014. 3D numerical reconstruction of well-connected porous structure of rock using fractal algorithms. Computer Methods in Applied Mechanics and Engineering, 279, 212-226. DOI: https://doi.org/10.1016/j.cma.2014.06.035

Kapur J.N., Sahoo, P.K., Wong, A.K.C., 1985. A new method for gray-level picture thresholding using the entropy of the histogram. Graphical Models and Image Processing, 29(3), 273-285. DOI: https://doi.org/10.1016/0734-189X(85)90125-2

Kittler, J., Illingworth, J., 1985. On threshold selection using clustering criteria. IEEE transactions on systems, man, and cybernetics, SMC-15 (5), 652-655. DOI: 10.1109/TSMC.1985.6313443

Li, B., Benson, S., 2015. Influence of small-scale heterogeneity on upward CO_2 plume migration in storage aquifers. Advances in Water Resources, 83, 389-404. DOI: https://doi.org/10.1016/j.advwatres.2015.07.010

Lin, Q., Al-Khulaifi, Y., Blunt, M.J., Bijeljic, B., 2016. Quantification of sub-resolution porosity in carbonate rocks by applying high-salinity contrast brine using x-ray microtomography differential imaging. Advances in Water Resources, 96, 306-322. DOI: 10.1016/j.advwatres.2016.08.002

Liu, N., Liu, M., 2016. Simulation and analysis of wormhole propagation by VES acid in carbonate acidizing. Journal of Petroleum Science and Engineering, 138, 57-65. DOI: https://doi.org/10.1016/j.petrol.2015.12.011

Mayo, S., Josh, M., Nesterets, Y., Esteban, L., Pervukhina, M., Clennell, M.B., Maksimenko, A., Hall, C., 2015. Quantitative micro-porosity characterization using synchrotron micro-CT and xenon K-edge subtraction in sandstones, carbonates, shales and coal. Fuel, 154, 167-173. DOI: https://doi.org/10.1016/j.fuel.2015.03.046

Otsu, N., 1979. A threshold selection method from gray-level histograms. IEEE transactions on systems, man, and cybernetics, 9(1), 62-66. DOI: 10.1109/TSMC.1979.4310076

Panga, M.K., Ziauddin, M., Balakotaiah, V., 2005. Two-scale continuum model for simulation of wormholes in carbonate

acidization. AIChE journal, 51(12), 3231-3248. DOI: https://doi.org/10.1002/aic.10574

Pini, R., Madonna, C., 2016. Moving across scales: a quantitative assessment of X-ray CT to measure the porosity of rocks. Journal of Porous Materials, 23, 325-338. DOI: https://doi.org/10.1007/s10934-015-0085-8

Rabbani, A., Jamshidi, S., 2014. Specific surface and porosity relationship for sandstones for prediction of permeability. International Journal of Rock Mechanics and Mining Sciences, 71, 25-32. DOI: https://doi.org/10.1016/j.ijrmms.2014.06.013

Rabbani, A., Ayatollahi, S., 2015. Comparing three image processing algorithms to estimate the grain-size distribution of porous rocks from binary 2D images and sensitivity analysis of the grain overlapping degree. Special Topics & Reviews in Porous Media: An International Journal, 6(1), 71-89. DOI: 10.1615/SpecialTopicsRevPorousMedia.v6.i1.60

Rabbani, A., Ayatollahi, S., Kharrat, R., Dashti, N., 2016. Estimation of 3D pore network coordination number of rocks from watershed segmentation of a single 2D image. Advances in Water Resources, 94, 264-277. DOI: https://doi.org/10.1016/j.advwatres.2016.05.020

Rabbani, A., Mostaghimi, P., Armstrong, R.T., 2019. Pore network extraction using geometrical domain decomposition. Advances in Water Resources, 123, 70-83. DOI: https://doi.org/10.1016/j.advwatres.2018.11.003

Ramandi, H.L., Mostaghimi, P., Armstrong, R.T., Saadatfar, M., Pinczewski, W.V., 2016. Porosity and permeability characterization of coal: a micro-computed tomography study. International Journal of Coal Geology, 154, 57-68. DOI: https://doi.org/10.1016/j.coal.2015.10.001

Rutqvist, J., Wu, Y. S., Tsang, C. F., Bodvarsson, G., 2002. A modeling approach for analysis of coupled multiphase fluid flow, heat transfer, and deformation in fractured porous rock. International Journal of Rock Mechanics and Mining Sciences, 39(4), 429-442. DOI: https://doi.org/10.1016/S1365-1609(02)00022-9

Schneider, C.A., Rasband, W.S., Eliceiri, K.W., 2012. NIH Image to ImageJ: 25 years of image analysis. Nature Methods, 9(7), 671-675. DOI: https://doi.org/10.1038/nmeth.2089

Smith, M.M., Hao, Y., Carroll, S.A., 2017. Development and calibration of a reactive transport model for carbonate reservoir porosity and permeability changes based on CO_2 core-flood experiments. International Journal of Greenhouse Gas Control, 57, 73-88. DOI: https://doi.org/10.1016/j.ijggc.2016.12.004

Spanne, P., Thovert, J. F., Jacquin, C. J., Lindquist, W. B., Jones, K. W., Adler, P. M., 1994. Synchrotron computed microtomography of porous media: topology and transports. Physical review letters, 73(14), 2001. DOI: https://doi.org/10.1103/PhysRevLett.73.2001

Steefel, C. I., Molins, S., 2016. CrunchFlow. Software for modeling multicomponent reactive flow and transport. User's manual (2016). Berkeley, Lawrence Berkeley National Laboratory, 91pp.

Steefel, C. I., Appelo, C. A. J., Arora, B., Jacques, D., Kalbacher, T., Kolditz, O., Lagneau, V., Lichtner, P. C., Mayer, K. U., Meeussen, J. C. L., Molins, S., 2015. Reactive transport codes for subsurface environmental simulation. Computational Geosciences, 19, 445-478. DOI: https://doi.org/10.1007/s10596-014-9443-x

Sutera, S. P., Skalak, R., 1993. The history of Poiseuille's law. Annual review of fluid mechanics, 25(1), 1-20.

Taron, J., Elsworth, D., 2009. Thermal–hydrologic–mechanical–chemical processes in the evolution of engineered geothermal reservoirs. International Journal of Rock Mechanics and Mining Sciences, 46(5), 855-864. DOI: https://doi.org/10.1016/j.ijrmms.2009.01.007

Tsai, W., 1985. Moment-preserving thresholding: a new approach. Computer Vision, Graphics, and Image Processing, 29(3), 377-393. DOI: https://doi.org/10.1016/0734-189X(85)90133-1

Vafaie, A., Soler, J.m M., Cama, J., Kivi, I. R., Vilarrasa, V., 2022. [CODE] A MATLAB code for digitized reconstruction of the rock porosity distribution from Computed Tomography (CT) images. Digital CSIC Library. Last accessed: 05/2024. Website: http://hdl.handle.net/10261/284837

Vafaie, A., Cama, J., Soler, J. M., Grgic, D., Vilarrasa, V., 2023a. Chemo-hydro-mechanical effects of CO_2 injection into a permeable limestone. International Journal of Coal Geology, 278, 104359. DOI: https://doi.org/10.1016/j.coal.2023.104359

Vafaie, A., Cama, J., Soler, J. M., Kivi, I. R., Vilarrasa, V., 2023b. Chemo-hydro-mechanical effects of CO_2 injection on reservoir and seal rocks: A review on laboratory experiments. Renewable and Sustainable Energy Reviews, 178, 113270. DOI: https://doi.org/10.1016/j.rser.2023.113270

Vanorio, T., Mavko, G., 2011. Laboratory measurements of the acoustic and transport properties of carbonate rocks and their link with the amount of microcrystalline matrix. Geophysics, 76(4), E105-E115. DOI: https://doi.org/10.1190/1.3580632

Voltolini, M., Ajo-Franklin, J., 2019. The effect of CO_2-induced dissolution on flow properties in Indiana limestone: An in situ synchrotron X-ray micro-tomography study. International Journal of Greenhouse Gas Control, 82, 38-47. DOI: https://doi.org/10.1016/j.ijggc.2018.12.013

Volume Graphics GmbH (2016). A New, More Compatible Software Generation: VGStudio 3.0, VGMetrology 3.0, and myVGL 3.0. e-Journal of Nondestructive Testing. https://www.ndt.net/?id=20203.

Wan, K., Xu, Q., 2014. Local porosity distribution of cement paste characterized by X-ray micro-tomography. Science China Technological Sciences, 57, 953-961. DOI: https://doi.org/10.1007/s11431-014-5513-5

Wenck, N., Jackson, S.J., Manoorkar, S., Muggeridge, A., Krevor, S., 2021. Simulating core floods in heterogeneous sandstone and carbonate rocks. Water Resources Research, 57(9), e2021WR030581. DOI: https://doi.org/10.1029/2021WR030581

Withjack, E. M., 1988. Computed tomography for rock-property determination and fluid-flow visualization. SPE

formation evaluation, 3(04), 696-704. DOI: https://doi.org/10.2118/16951-PA

Wu, Y., Lin, C., Yan, W., Liu, Q., Zhao, P., Ren, L., 2020. Pore-scale simulations of electrical and elastic properties of shale samples based on multicomponent and multiscale digital rocks. Marine and Petroleum Geology, 117, 104369. DOI: https://doi.org/10.1016/j.marpetgeo.2020.104369

Yen, J.C., Chang, F.J., Chang, S., 1995. A new criterion for automatic multilevel thresholding. IEEE Transactions on Image Processing, 4(3), 370-378. DOI: 10.1109/83.366472

Zhang, T., Du, Y., Huang, T., Yang, J., Lu, F., Li, X., 2016. Reconstruction of porous media using ISOMAP-based MPS. Stochastic environmental research and risk assessment, 30, 395-412. DOI: https://doi.org/10.1007/s00477-015-1142-1

Manuscript received June 2023;
revision accepted May 2024;
published Online June 2024.